Role of the local stress systems on microstructural inhomogeneity during semisolid injection

S. Bhagavath[1,2], Z. Gong[2,3], T. Wigger[2,3], S. Shah[2,3], B. Ghaffari[4], M. Li[4], S. Marathe[5], P.D. Lee[2,3+], S. Karagadde[1+]

[1]Department of Mechanical Engineering, Indian Institute of Technology Bombay, Mumbai 400076, India

[2] Research Complex at Harwell, Harwell Campus, OX11 0FA UK

[3]University College London, London WC1E 6BT, UK

[4]Ford Research and Advanced Engineering, Dearborn, USA

[5]Diamond Light Source, Harwell Campus, OX11 0DE, UK

[+] Corresponding authors: s.karagadde@iitb.ac.in, peter.lee@ucl.ac.uk

Abstract

High pressure metal die casting is an extremely dynamic process with widely ranging cooling rates and intensifying pressures, resulting in a wide range of solid fractions and deformation rates simultaneously existing in the same casting. These process parameters and their complex interplay dictate the formation of microstructural solidification defects. In this study, fast synchrotron X-ray imaging experiments simulating high pressure die casting of aluminium alloys were conducted to investigate the effect of solid fraction, loading conditions and semisolid flow on local microstructural inhomogeneity. While most of the existing literature in this field reports speeds up to 10 µm/s for *in situ* deformation, the present work captures much faster filling and solidification, at speeds closer to 100 µm/s and at different solid fractions. Semisolid deformation of low solid fractions reveals two typical microstructural features: (i) coarser grains in the middle and finer ones near the walls, and (ii) remelting near the solid-liquid interface due to Cu enrichment in the liquid by the flow. *Ex situ* scans and digital image correlation analysis of the higher solid fraction samples reveal a porosity formation mechanism based on the local state of stresses, microstructure and feeding. Four different characteristics were identified: (i) plug flow, (ii) dead zone (densified mush), (iii) shear and (iv) bulk zones. These insights will be used to develop zone-specific strategies for the numerical modelling of defect formation during die casting.

Key words: Semisolid; Dilatancy; X-ray radiography; Digital image correlation; Microstructural response

1. Introduction

Metal casting is a widely utilised process for manufacturing near-net shapes from liquid melt. In some special classes of metal casting, additional pressure is applied during solidification. Among these, High Pressure Die Casting (HPDC) is an expedient technique for producing non-ferrous alloy components at a rapid production rate. During the HPDC process, liquid melt is injected at speeds in the range of ~40-60 m/s and cooled at rates of approximately 10^2-10^3 K/s, while maintaining an intensification pressure up to 80-100 MPa [1,2]. Moreover, HPDC cast components are often intricate shapes with sections varying from ~1 millimetre to several centimetres [2]. Due to the varying thickness across the cast component, the local cooling rate and thus the local solid fraction changes. This affects the local permeability [3,4] and the composition of the semisolid mushy zone, i.e. mush and hence its response under external pressure [5,6]. As a consequence, a number of porosity defects [7] occurring that are related to filling, thermal contraction [5] and segregation bands (eutectic and porosity) [8–11] can be traced to the extreme thermo-mechanical and microstructural conditions prevailing at higher solid fractions in these zones. It is estimated that about ~35% of casting defects in HPDC components are porosity [12]. These porosity defects severely limit the usability of HPDC products, as they may initiate fatigue failure [13].

Earlier research on understanding the porosity mechanisms focused on the formation of gas and shrinkage pores using post-mortem observations [14,15]. Lee and Hunt [16] conducted the first *in situ* observation of porosity in Al-Cu alloys using an X-ray temperature gradient stage and quantified the role of the cooling rate on the pore radii and the volume fractions. Subsequently, several directional solidification experiments focusing on the hydrogen micro-porosity formation have been conducted [17,18] revealing the role of gas diffusion on growth. Based on these radiographic observations, empirical models of pore growth accounting for the influence of hydrogen diffusion [19], volumetric shrinkage [20] and microstructural features like intermetallics [21] have been reported. The primary studies on the shrinkage porosity focused on the permeability and lack of feeding [22,23]. Recently, due to the equiaxed nature of HPDC microstructure and the densification of the solid under loading, the granular mechanics theory [7,24] has been widely adapted to model the solidification and shrinkage formation in HPDC [25,26]. Gourlay et al. [8,9,27] in their foundational papers reported a mechanism for the formation of shrinkage bands due to dilatancy by considering the solid as a granular medium. They further studied the role of Externally Solidified Crystals (ESC) in shrinkage band formation [28], reporting that the migration of ESCs toward the geometric centre (in case of symmetrical casting) increased the local solid fraction whilst affecting the position and nature of segregation bands in Mg-Al alloys. However, these studies did not account for the role of the combined effect of various deformation forces and their influence on pore nucleation and growth mechanisms. Also, the role of the geometry was not considered in these studies. Recently, Li et al. [29] investigated the influence of melt flow and ESCs on the formation of defect bands near the gate in HPDC of a AZ91D magnesium alloy. The defects were found to be along the cross-section where the narrow gate region opens to a wider die. They proposed a mechanism for shrinkage pore formation based on the shearing of ESCs from bulk liquid flow and allowing pore nucleation in intergranular region.

Recent advances in synchrotron technology have enabled time-resolved visualisation of the semisolid deformation process [10,30], providing further insight into the shear shrinkage bands caused by stress-induced dilation. Cai et al. [31] and Kareh et al. [10] were the first to examine volumetric dilation induced segregation of inter-dendritic liquid as a response to the compression of semisolid Al-Cu, *in situ*. Cai et al. [31] defined three regimes of pore growth during semisolid deformation and reported the enhancement of porosity growth due to dilatancy. Semisolid extrusion and indentation experiments showed inter-dendritic liquid segregation as a response to volumetric dilation [32–34]. Bhagavath et al. [35] reported the existence of dilatancy-induced convection-driven gas pore growth under compressive forces. Recently, Su et al. [36] conducted *in situ* experiments to study the shift of the flow regime, from a suspension to granular type, during the semisolid deformation experiments. They estimated the change in liquid pressure at the first point of cracking. These radiographic experiments, along with numerical results using a coupled Discrete Element Method- Lattice Boltzmann Method (DEM-LBM) model and Digital Image Correlation (DIC) measurements, highlight the role of solid fraction and shear strain rate on cracking [36,37]. However, the transport phenomena involving eutectic liquid convection are not sufficiently explored, and to understand the volumetric dilation induced porosity bands, a thorough understanding of porosity and band defects is required.

Most of the previous work on semisolid deformation is based on the response of the semisolid network subjected to uniaxial loading conditions (tensile, compression, shear) in binary alloy systems of uniform cross-section [33,38,39]. These simple systems do not account for the local changes in cooling rates and flow, as seen in castings with varying thicknesses. Moreover, due to the limitations of the synchrotron image capturing capabilities, many of the synchrotron studies were limited to a maximum deformation rate of 10 μm/s. Thus, for results more representative of actual applications, trials need to be conducted with the maximum imaging, cooling, and flow rates experimentally achievable, to surpass past experiments and to investigate a previously unexplored regime.

During the HPDC process, the feeding pressure in liquid pockets can be blocked by localized solidification, with various sections subjected to different orders of cooling and deformation rates. To understand the underlying mechanisms of defect formation in HPDC components and to mimic the interplay between multiple stress conditions, such as bulk flow, thermal stresses and the injection pressure acting over a range of solid fractions, radiographic experiments at sufficiently high image capture rate are necessary. The experiments also need to take into account the effects of varying casting thicknesses, and thus the cooling conditions on the propensity of crack nucleation and growth. In this study, for the first-time time-resolved *in situ* X-ray radiographic injection experiments on Al-10 wt.% Cu and a modified ADC12 alloy enriched with copper were performed using a T-shaped die with a narrow constriction section opening to a wider die region. The filling processes at two different initial solid fractions of ~50% and ~75% injected at 80 µm/s were investigated, and the mechanisms of the deformation response were examined. The samples were characterised post-mortem in 3D to quantify the pore distribution in the sample, and DIC was used to measure principal strains. At lower solid fractions, the various stages of deformation were analysed. For experiments performed at high solid fractions, solid fractions and flow zones with different microstructural properties were defined based on local stress conditions. These qualitative and quantitative process maps will be used to design zone-specific numerical models for HPDC casting and shed light on the effect of cross-sectional changes on pore formation.

2. Materials and methods

2.1 Sample preparation

Based on the results of preliminary laboratory experiments, two alloy systems, Modified ADC12 and Al-10 wt.% Cu (herein referred to as MADC12 and Al10Cu, respectively), were chosen for the synchrotron experiments. The MADC12 alloy is a traditional ADC12 die-cast alloy with additional Cu to enhance the attenuation contrast between the phases (see Table 1 for the composition). The samples were prepared by melting the alloy ingots in a PID-controlled coreless induction furnace, in an 80 mm diameter stainless steel crucible. The samples were heated to about 20 °C above the melting point (superheat), stirred thoroughly with a graphite rod and then quenched in a water bath. The cylindrical cast sample was 20 mm in height and 80 mm in diameter. The ambient temperature and humidity conditions (RH ~60%) were maintained during the casting of different alloy systems.

Table 1: Alloy composition in wt.% analysed by Inductively coupled Plasma-Atomic emission spectroscopy (ICP-AES) and Energy-Dispersive X-ray spectroscopy (EDX). The balance in both cases is aluminium.

Sample	Cu (wt. %)	Fe (wt. %)	Si (wt. %)
Modified ADC12	10.43	0.80	10.5
Al-10Cu	9.82	0.60	0.50

The samples were then machined using wire Electrical Discharge Machining (EDM) into flat rectangular samples of 11×12 mm^2 cross-section and 1 mm thickness. The edges were smoothened using 320 grit emery paper to avoid high-stress concentrations, thus ensuring the piston did not crack under heavier loads. The samples were then carefully tapered at the bottom end for transition fit of the sample inside the hollow piston, which features a 1 mm wide cavity matching the sample thickness (Figure 1(a)). The machined samples were placed inside the piston, ensuring the alignment of the top surfaces of the sample and piston. They were designed to fit tightly with no sideways movement possible.

After heating the assembly to the desired temperature (furnace is shown in Figure 1(b)), a vertical load was applied using a second alumina die with a cavity (Figure 1(a), top), which slides into the lower part whilst deforming the sample. The die cavity is designed in the shape of a "T", with a 3 mm wide constriction region (CR) and a 6 mm wide 'Thicker region' (TR) (see Figure 1(a)). The height of the cavity is 2.5 mm.

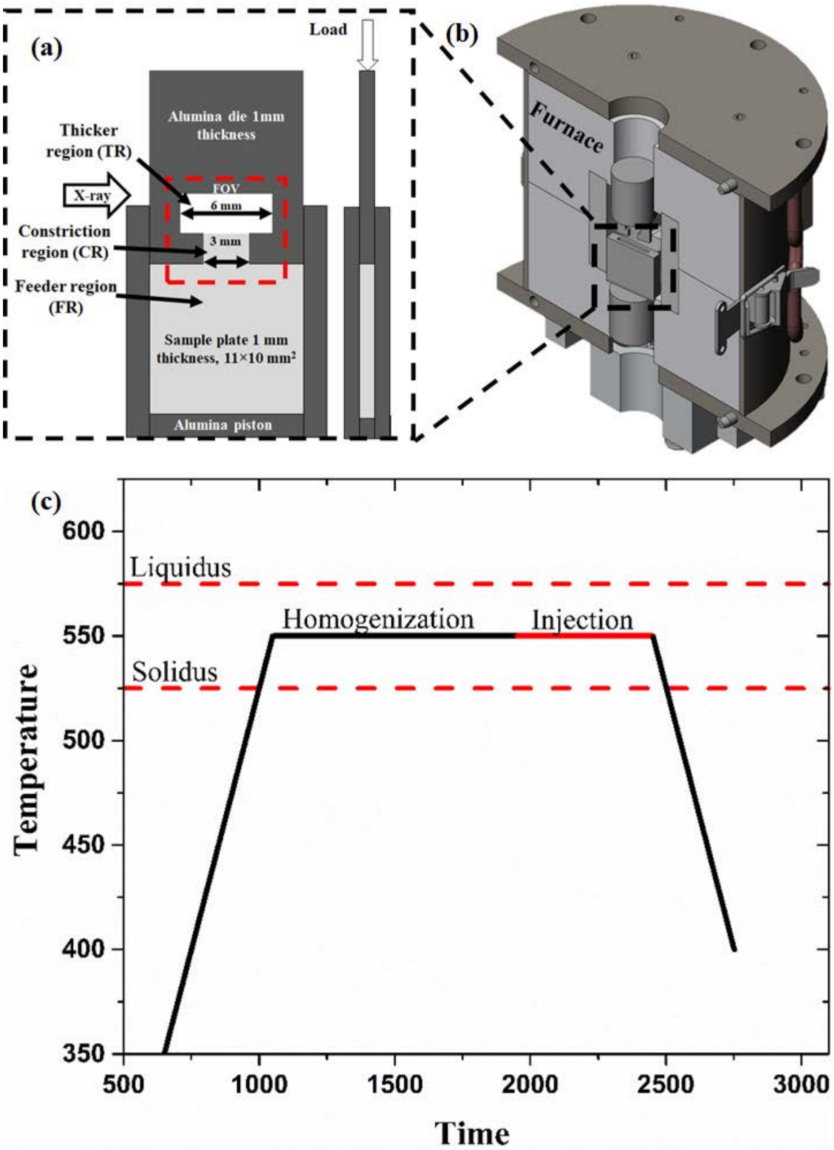

Figure 1: (a) Illustration of the sample (light grey) mounted in the custom alumina die-piston combination (dark grey). (b) Alumina and sample are placed between the rams of the P2R loading rig inside the resistive-heated furnace. (c) Example of the sample temperature profile during the injection experiments, in which the heating and cooling rate were maintained at 0.4 °C/s.

2.2 *In situ* radiographic investigation of injection and solidification

The fast synchrotron experiments were conducted on the I13-2 beamline of Diamond Light Source [40–42] (beamtime reference MG22053). A schematic of the beamline arrangement is shown in supplementary Figure S1. The custom-built, PID-controlled resistance-heated furnace (see supplementary Figure S2) featuring an 8×8 mm^2 X-ray transparent window (Figure 1(b)) mounted on a bespoke mechanical rig (P2R) [43] was used for the injection-solidification experiments. This mechanical test setup has been used to conduct a wide range of thermo-mechanical experiments [43]. The mechanical rig has high precision loading control (as low as 100 nm/s) and force measurement (better than 0.1 N).

The temperature vs. time profile followed during the deformation experiment is shown in Figure 1(c). The sample was heated at 0.4 °C/s until the pre-determined isothermal temperature corresponding to an estimated solid fraction was reached (heating stage). The specimen temperature was calibrated offline by placing a thermocouple in contact with the sample inside the alumina piston before the deformation experiments (supplementary Figure S3). The temperature vs. solid fraction was estimated based on the measured furnace temperature using the Scheil solidification module of ThermoCalc®. The liquidus and solidus temperatures were further verified by Differential Scanning Calorimetry (DSC) (supplementary Figure S4). The sample was held at the highest temperature for 10 minutes to attain a homogeneous state (homogenisation stage). The die was then pushed downwards into the piston, deforming the sample until the load reached a limit of 400 N (limit set to safeguard the mechanical apparatus), followed by cooling at a rate of 0.4 °C/s (cooling stage).

A pink X-ray beam with an energy of 27 keV was used. During the deformation and cooling stage of each experiment, a set of 6000 radiographs was acquired using a PCO.Edge 5.5 camera coupled with camera module 1 [42]. Radiographic images with a size of 2560×2160 pixels were obtained with a pixel size of 2.6 µm, corresponding to an effective field of view of 6.7 mm × 5.6 mm [40,41]. The exposure time was kept at 50 ms. The images were initially corrected using flats and darks taken before and after the experiments. The 6000-image stack was further de-noised using a 2D median filter with 3 pixels radius and cropped to appropriate sizes, removing the areas showing only alumina die and piston. For the segmentation of pores, the trainable Weka segmentation plugin [44] in Fiji ImageJ [45] was used.

After the *in situ* experiments, the deformed samples were characterised further in 3D using high-resolution lab X-ray tomography (Nikon XTH, 225, UCL Centre for Correlative X-ray Microscopy). Per tomogram, 3185 projections were taken over 360° at an effective pixel size of 7.96 µm. The tomographic images were segmented to quantify the pores and solid networks, using the same machine learning-based Weka segmentation plugin, as above in Fiji. An open-source 3D slicer was used for volume rendering [46]. For the 2D and 3D quantification of the pores measured, the 3D count label and morpholibj plugins [47] of ImageJ were applied.

3. Results and discussions

3.1 Low solid fraction injection

Time-resolved radiographic images showing the *in situ* deformation of the low solid fraction (~50%) Al10Cu sample, injected at a loading rate of 80 μm/s, are shown in Figures 2(a-d). Figure 2(a) illustrates the state of the sample at the end of the heating (574 °C sample temperature) and homogenisation stages of the experiment (note that the image has been registered and cropped to maintain the die position in the image sequence). Based on the greyscale, three phase features were identified as solid *α* phase, liquid phase, and pores. A lighter grey shade indicates pre-existing pores (including the air ahead of the solid interface) or pores generated during the heating stage, whilst medium and darker shades indicate the solid α and liquid phases, respectively. The white region on top of Figure 2(a) has been cropped to maintain a fixed position of the die position in the image. At this stage of the experiment, the distribution of the various phases is stochastic with no evident phase segregation, suggesting that buoyancy forces can be ignored.

On applying the load, the semisolid enters the narrow constriction region traversing with a nearly flat interface. By measuring the position of the interface, the velocity was found to be 29.6±0.2 μm/s. This system is analogous to plug flow seen during semisolid extrusion of non-Newtonian fluids like Bingham plastics [48,49]. The plug flow behaviour depends on the strain rate, which affects the effective viscosity, and persisted for all the loading rate conditions in the experiments. The wall friction effect was found to be minimal, probably due to a thin layer of liquid alleviating the frictional effects.

Due to the effects of squeezing action by the compressive forces, the region just below the die is found to be depleted of inter-dendritic liquid (left and right sides below the die, Figure 2 (b)). The compressive forces squeeze the inter-dendritic liquid toward the central die opening, further enhanced by the suction caused by the volumetric dilation. The region below the ceramic wall at the constriction zone is subjected to shear due to the downward movement of the die. The increased volumetric strain due to this shear induces a negative pressure, which draws in the inter-dendritic liquid from the neighbouring compressed dead zone. This liquid network formation due to volumetric dilation has been previously reported for semisolid tensile, compression, and extrusion experiments for Al-Cu binary alloy systems [31,35].

On the continuation of loading (Figure 2(c)), the liquid front moves upwards ahead of the solid network. Due to the relatively higher density of copper compared to aluminium, it is evident from the images that this liquid is enriched in copper, compared to the initial composition. The tomograms of the deformed sample were cropped into several smaller volumes for estimating the copper concentration. These 3D volumes were then segmented to find the fraction of α aluminium and liquid. By back calculation and using the Lever rule, the copper concentration is estimated to be 29%. With the rising liquid, tiny hydrogen gas [50,51] pores squeeze through the solid network, rising to the liquid-air interface and escaping to the atmosphere. During deformation, the gas pores which are trapped in the solid network grow according to the diffusion laws [19,52] (deformation and solidification driven). The required flux is provided by hydrogen convected from the rising liquid [35]. During the cooling stage (Figure 2(d)), the pores grow further, initially due to the influx of hydrogen partition from the solid and later by the shrinkage forces.

After the deformation is completed, dendrite fragmentation, followed by remelting was observed at the interface of extruded solid and liquid, as observed from the change in grey scale intensity from lighter (solid) to dark (liquid) (shown in green circle in Figure 2(e-g). This is attributed to the conservation of local species concentration, which is re-distributed due to the copper-rich liquid layer [51] (Figure 2(e-g)). The mechanism behind the remelting is illustrated in Figure 2(h). The copper concentration at the interface of solid mush and the exudated liquid (C_l=29.06 wt.%) is considerably larger than in the mush (C_0=10 wt.%), without considerable temperature differences across, indicating near isothermal deformation. A local equilibrium can be achieved by either remelting of the solid (which is lean in solute) or diffusion of the species to the solid [51]. As the rate of species diffusion is considerably lower compared with the bulk motion of the semisolid, the solid mush starts re-melting due to the influx of copper rich liquid.

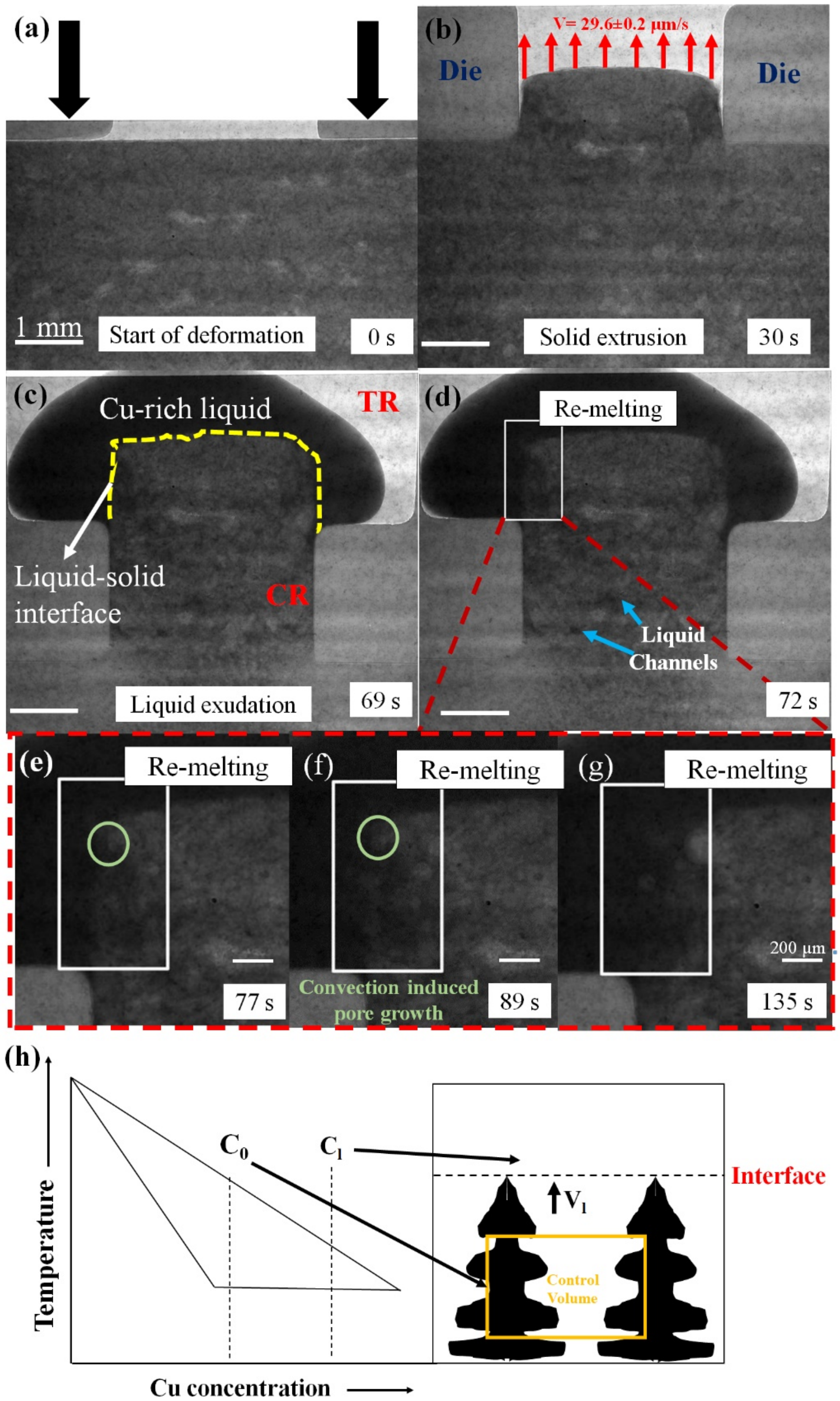

Figure 2: Time-resolved radiographic images (a) just before the application of load; with the loading direction is shown as black arrows, (b) extrusion of the solid network, (c) Copper-rich liquid exudation, (d) start of the remelting during the deformation process of Al10Cu alloy. (e-g) show a magnified view of the evolution of interfaces during the remelting process (supplementary video 1). (h) Simplified phase diagram illustrating the mechanism for the remelting phenomenon. The scale bar for figures (a-d) measures 1 mm and for (e-g) measures 200 μm.

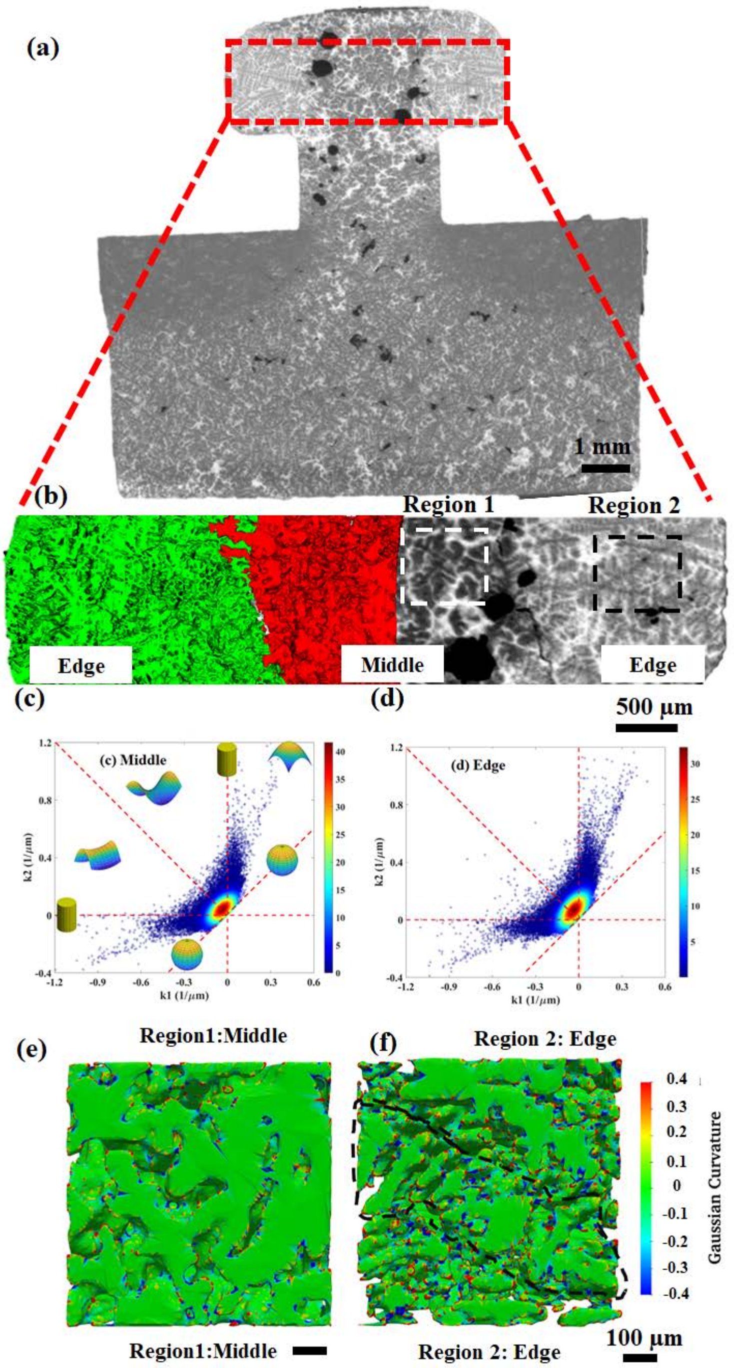

Figure 3: (a) Vertical tomographic slice of the sample. Note that the representative slice is taken at the axisymmetric plane along the thickness, (b) Magnified view of the TR (see Figure 1(a)) of the solidified sample and the corresponding 3D rendering (parallel to loading axis) showing the microstructural changes between the extruded solid (shown in red) and the copper-rich liquid region (shown in green). ISD plots highlighting the distribution of principal curvatures for (c) Region 1 (middle) and (d) Region 2 (edge) shown in (b). Distribution of Gaussian curvature of (e) middle and (f) side section for the 50% semisolid Al10Cu loaded at 80 µm/s.

A tomographic slice of the sample along the loading direction, post deformation is shown in Figure 3(a), whilst Figure 3(b) depicts a magnified view of the 3D structure in the top region, with a corresponding vertical tomographic slice of the sample in the die (TR). To characterise the coarse and fine grain structures, the local principal curvatures were measured and plotted as Interfacial Shape Distribution (ISD) graphs [53,54]. The principal curvatures *κ1* and *κ2* are defined as the reciprocal of principal radii R_1 and R_2. ISD plots are commonly used to represent the coarsening of dendrites, as the shape features described by the plots are used to define various morphological features in dendrites [55]. For example, a saddle shape indicates a region connecting two secondary/ternary dendrites; elliptic shapes represent dendrite tips and hyperbolic shapes indicate dendrite branches.

The ISD plots at the end of deformation and cooling are shown in Figure 3(c-d) for the middle and edge sections, respectively. The colour red in the figure indicates the highest probability of the solid-liquid interfacial shape. The two main branches are aligned along $\kappa_1 = \kappa_2 = 0$, indicating a flatter morphology. The highest probability region for edges was found to incline away from the elliptic shape moving towards the $\kappa_2=0$ line. This is an indication for the start of dendrite coarsening and filling of the space between secondary arms. Since the liquid is rich in copper, the solidification range and, consequently, the solidification time is small, resulting in only limited coarsening (Figure 3(f)) compared with more coarsening in the middle (Figure 3(e)). The dendrites hence mostly fit a paraboloid shape [55]. The grains in the middle region are pre-existing (pre-melting), and even though they are slightly coarsened during cooling, the general trends are not conclusive, as the shape of the grains is not only affected by solidification but also deformation. It is to be noted that the ISD plots indicate a general qualitative trend of the curvature distribution, as it is strongly influenced by the image segmentation.

In a casting process such as HPDC, low and high solid fraction regions exist simultaneously due to the variations in cooling rates from wall to the centre. Accordingly, the semisolid mush and resulting microstructure can vary substantially with solid fraction. In the next section, the details of the semisolid response and defect formation at higher solid fraction are given.

3.2 High Solid fraction injection

In the case of the high solid fraction mush, deformed at 80 µm/s (Figure 4 (a-c)), cracks start to appear in the constriction region (Figure 4(b)) from the instant of load application. The cracks are mostly observed to be aligned along the loading axis. In the feeding region (Figure 1(a)) at the sample bottom, the nucleation of porosity is caused by shearing due to the opening of solid networks and volumetric dilation. The cracks in the CR open because of the lateral strain developed in the moving semisolid plug flow. Note that the experiments were stopped as soon as the load reached a maximum of 400 N. In high solid fraction case, this occurs early when the semisolid enters the constriction region, and thus, its behaviour in the thicker region could not be observed.

To determine the force distribution, the stacks of radiographs were subjected to a DIC routine using the Ncorr plugin [56] in Matlab® 2018a. The images were cropped to focus on the deforming regions and the image was filtered using anisotropic diffusion filtering to reduce noise, as shown in Figure 4(d-f). Corresponding DIC images are shown in Figure 4(g-i), where the red and blue colours indicate strains in opposing directions perpendicular to the loading axis. The DIC analysis reveals the development of large shear and lateral strains (perpendicular to the loading axis) as the solid enters the constriction region (CR) due to friction at the ceramic wall. This causes the nucleation and growth of pores in this region, as discussed in section 3.3.

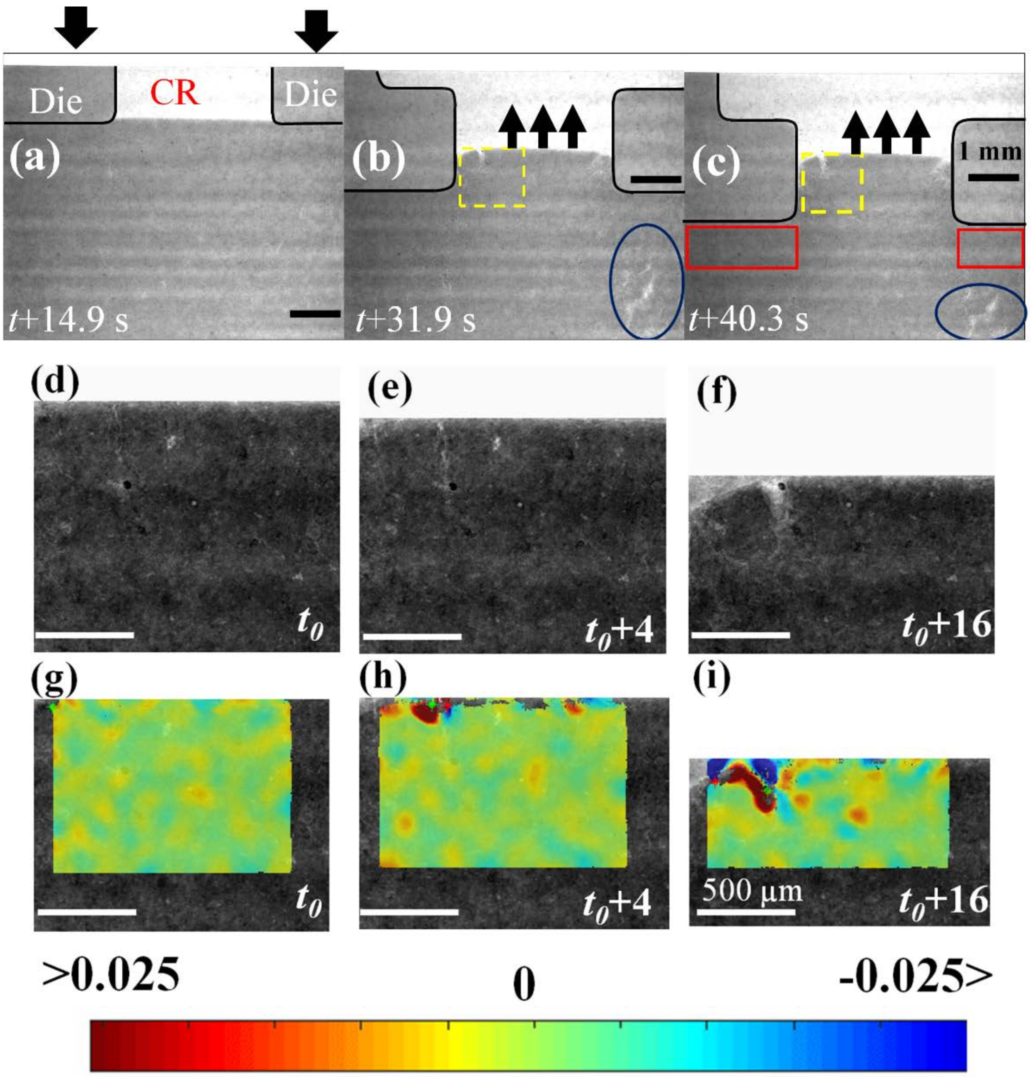

Figure 4: (a-c) Radiographic slices showing the evolution of pores and cracks during the deformation of Al10Cu. The red boxes indicate the dead zone, and the blue ovals indicate shear cracks. (d-f) Enlarged view of the pores at the interface in the yellow box in (b-c). (g-i) DIC images showing strain maps of the same

region, highlighting the role of shear and lateral strains in pore opening. Note that the contrast is adjusted in images (d-f) to improve the DIC results. Note that scale bar for Figures (a-c) measures 1 mm and for (d-i) measures 500 µm.

The *in situ* radiographs of the sample in Figure 5(a-c) show pre-existing pores already prevailing in the material before deformation. In this case, the cracks are oriented perpendicular to the loading direction, following the path of least resistance along the pre-existing pores. The change in pore fraction and the largest and smallest dimensions of the near-elliptical pores (major/minor axis lengths) with deformation time are shown in Figure 5(d) (see supplementary information 5 for ellipse fit). The major axis length and pore fraction increase initially with the applied load, reaching a maximum at about 4.25 s and 5.5 s, respectively, from the beginning of the measurement. Both decrease and plateau thereafter at ~ 1640 µm major axis length and ~26.9 % pore fraction at 8.5 s and 9.5 s, respectively. The decrease in the major axis length is attributed to the reactive forces that have developed as a consequence of wall friction, as seen from the DIC results of the specimen with no pores. DIC estimation of the shear strain with pore is given in supplementary Figure S5, which is in good agreement qualitatively, with the case without the pre-existing pores.

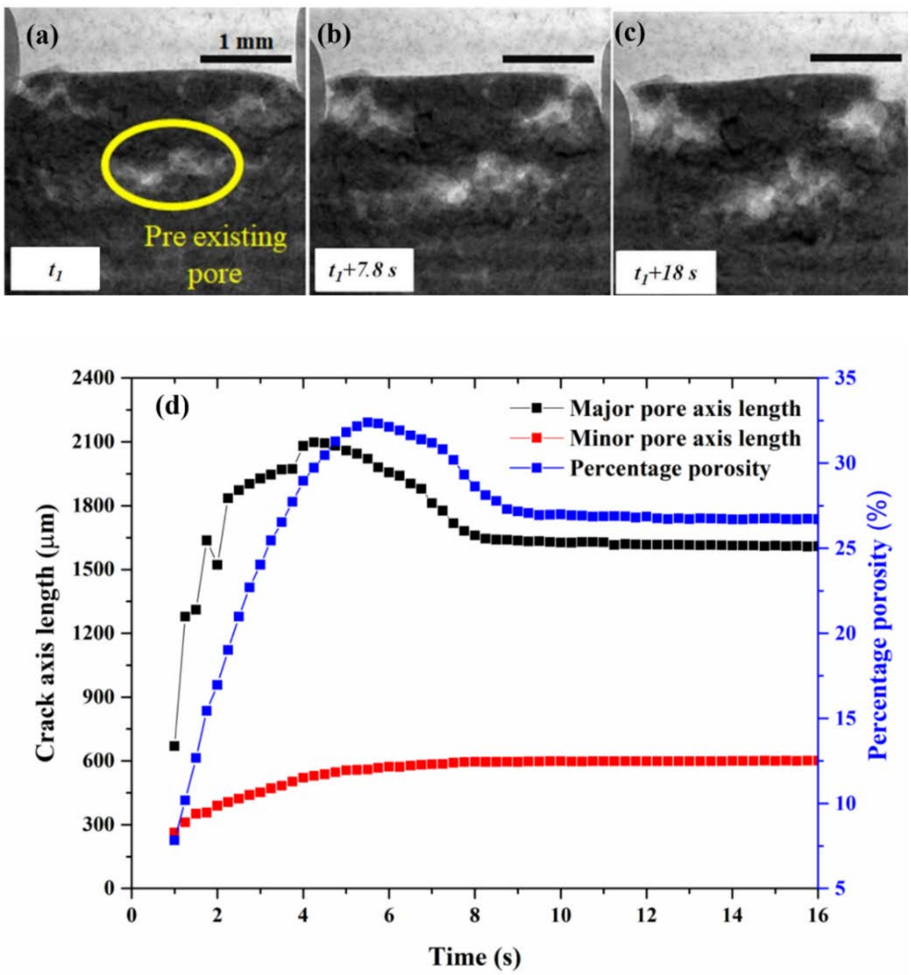

Figure 5: (a-c) Radiographic slices showing the evolution of pores and cracks during the deformation of Al10Cu with a pre-existing pore (based on trial 1 in Figure 6) (see supplementary video 2) (d) Temporal evolution of major and minor crack length and area fraction of pore (pre-existing pore). Note that the scale bar for figures (a-c) measures 1 mm.

As seen from the two cases, for the prediction of porosity in HPDC, it is critical to consider the stresses acting on the mush and the pre-existing pores or particles and the interaction of the dendrites with the die wall. The local forces systems are determined by the dilatancy, friction between die wall and the melt along with the bulk force due to injection.

3.3 3D characterisation of the deformed sample

Post deformation, a tomography scan was performed on the high solid fraction specimen. The area pore fraction was integrated over horizontal slices across the whole width of the sample, in 292 steps along its height in loading direction, as shown in Figure 6(a). Three Al10Cu samples were injected at a velocity of 80 µm/s for this study. The pore fraction vs. normalised height curves are characterised by two distinctive peaks and a drop in between. Based on the variation of the pore area fraction, the deformed sample has been divided into three sections A, B, C. The experiment was repeated on a MADC12 alloy showing similar behaviour (see supplementary Figure S6). Note that, in the trial represented by the black curve (trial 1) and a blue curve (trial 2), an additional peak appears in the region left of zone C. As discussed earlier, we have slightly tapered the sample to accommodate for tolerance for machining the ceramic surfaces at the bottom of the piston. Despite the taper, the sample movement may be obstructed locally due to surface imperfections. The sharp peaks may hence be attributed to temporarily occurring higher loads in these regions.

Region A- Plug flow zone

In Figure 6(b), the red and blue arrows indicate the inter-dendritic flow induced by compression and volumetric dilation, respectively. Whilst the convected liquid forms isolated liquid pockets, the pore formation in these pockets is due to the coupled action of volumetric dilation, compression, and rising gas bubbles convected by the liquid [35]. The pore sizes are considerably larger compared to the other sections. The deformation process has been explained in section 3.2. Two types of pore formation mechanisms are seen in this zone that can be explained as follows:

(a) Shearing of the network by the extrusion: Due to the pulling action caused by the flow of semisolid into the constriction from the feeder zone, pores perpendicular to the loading axis were developed. Phillion et al. [57] conducted tensile experiments of an Al-Cu alloy and have reported the mechanism for liquid localisation and/or pore formation. The pores located along the perpendicular direction to the loading axis observed were of this kind. The mechanism is similar to the case of low solid fraction injection explained in section 3.1. The notable difference between the two cases is that the channels formed in this case are relatively thinner, and due to the high solid fraction and thus low permeability, are the location of the shrinkage pores.

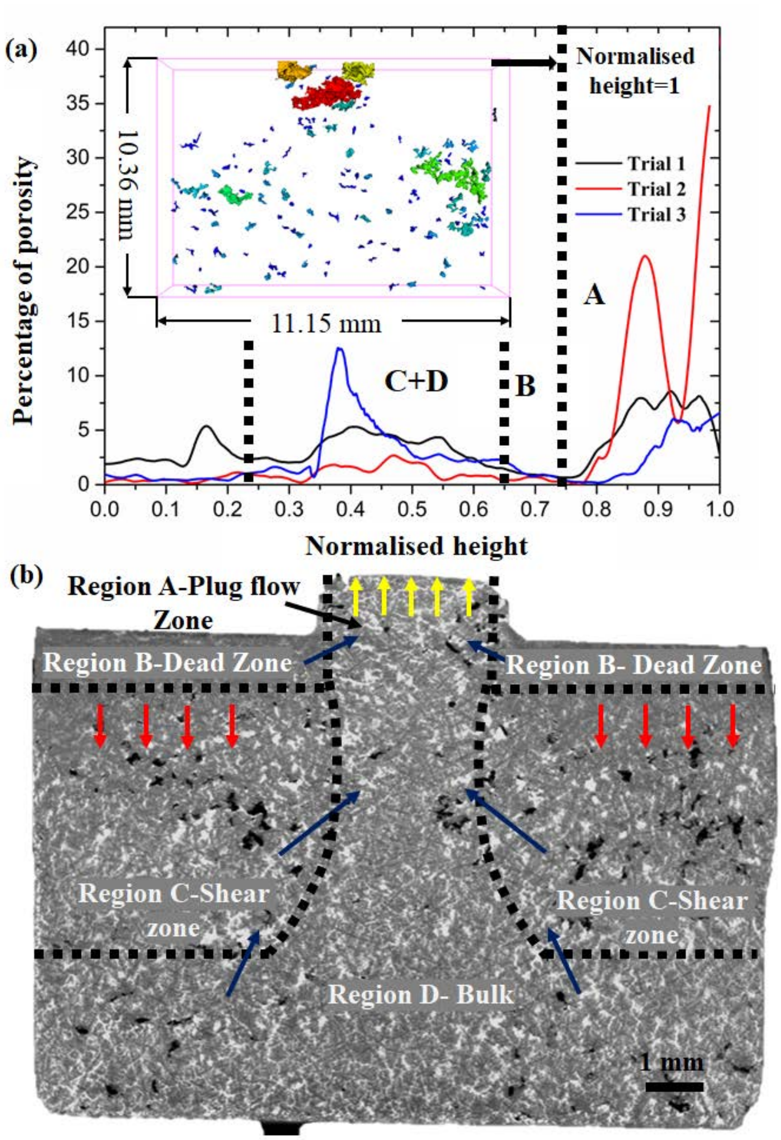

Figure 6: (a) Porosity quantification along the height of the high solid fraction sample deformed at 80 µm/s. The inset shows a 3D volume rendering of the pores in one of the three samples, which is colour coded to show their size, with red indicating the largest pores and blue the smallest. (b) Division into zones based on the local pore and liquid fraction in which blue and red arrows indicate feeding due to dilation and compression, respectively.

(b) The semisolid velocity profile in the constriction zone is characteristic for plug flow. However, due to the friction between the die and the dendrites close to the wall, the layers close to the wall have a lower velocity than the front. The differential velocity between these two layers induces a shear force. Depending on the permeability, this leads to the development of dilatant eutectic bands or a shear crack from the surface. The mechanism for the crack nucleation and growth is shown in Figure 7 (a-b). The frictional effects at the wall, influence the flow profile near the walls resulting in the nucleation and growth of cracks on the solid-liquid interface.

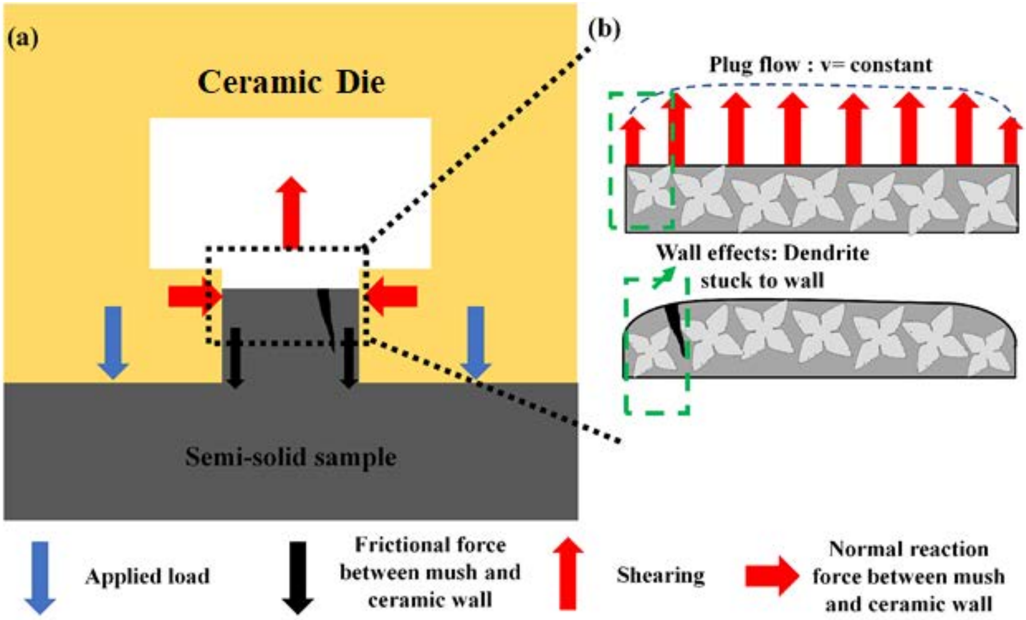

Figure 7: (a) Mechanism for crack initiation and growth due to combined reaction and shearing in the constriction region. (b) Magnified view showing the shear-induced crack developed during the plug flow of the semisolid.

It should be noted that trial 2 was associated with a significantly higher pore fraction in zone A (from ~10% to ~40%) (explained in section 3.2). This was due to the presence of pre-existing pores (pre-melting), whose growth was accelerated by the forces. In cases where there are no pre-existing pores present, the pore fraction for two alloys, Al10Cu and MADC12, is comparable (Supplementary Figure S6).

Region B- Dead zone

The region B is characterised by a low pore and eutectic liquid fraction. The liquid in this zone is squeezed in and segregates around the neck and lower-middle region. Since the applied compression is high in the region just below the piston, the solidified skeleton could not withstand the load and has collapsed. Under such conditions, 'burst feeding' is known to occur [15]. It has been reported that during the semisolid compression, the voids initially get compressed, followed by liquid channel formation and crack growth. However, in this case, as the liquid was already depleted, a highly porous solid structure was formed. This foamy structure absorbs the load, thereby reducing the compression forces acting on zone C. Thus, the pressure acting on zone C is not high enough to break the solid barrier but facilitate the liquid flow due to dilatancy.

A similar liquid-depleted dead zone and porous solid mush are seen in the MADC12 alloy shown in the inset of supplementary Figure S6. The dead zone is found to be asymmetric with a larger liquid depletion on the left side of the piston compared to the right. This indicates that the force applied on the left is higher, attributed to the irregularity on the ceramic piston wall.

Region C and D- Shear zone and the bulk semisolid

The region below the dead zone can be divided into two zones, shear zone (region C) at the edges and bulk semisolid (region D) in the middle. As discussed in section 3.1, the liquid from the dead zone is squeezed down to region C. As a consequence of the downward movement of the die, a region of high shear stress develops along the die-constriction zone interface. To alleviate the stress, the eutectic-rich liquid is drawn from zones B and D. When this feeding of the liquid is cut off due to the decrease in permeability, and cracks start to nucleate to compensate for the lack of feeding. Also, as the copper-rich liquid is the last solidifying region, the eutectic band of the liquid becomes the site for shrinkage pores (dilatancy and volumetric shrinkage dependent). The cracks formed due to shearing action further act as a nucleating zone for these shrinkage pores. The feeder region, adjacent to zone C and below the constriction zone, is not subjected to the compression as seen in the dead zone. This region is not affected by the applied loading, and the response of this region is similar to undeformed bulk semisolid.

A mechanism of the pore formation based on the local solid fractions and stress-state is illustrated in Figure 8. An optical micrograph of the various zones described in the Figure 8, showing the post-scan microstructure is provided in supplementary Figure S7. The mechanisms highlight the role of stress systems, varying cross-section and local solid fractions on the defect formation. As a response to the applied injection force, the three sections of the T shaped casting, feeder region, constriction region and thicker region, are subjected to various loading conditions. These loading conditions are influenced by the changing local solid fractions and the flow profile and velocity. Four distinct zones are identified, (i) plug-flow zone, (ii) dead (mush densification) zone, (iii) high-shear zone, and (iv) compression zone. The forces were mainly compressive in the dead zone, and the region was characterised by a compact solid network with fine pores. The solid network moves with a flat velocity profile at the centre with reduced velocities at the walls in the plug flow zone. The high shear created by the flow and dilation leads to the formation of isolated liquid channels and pores. The zone C experiences shear along the edges due to the movement of the die.

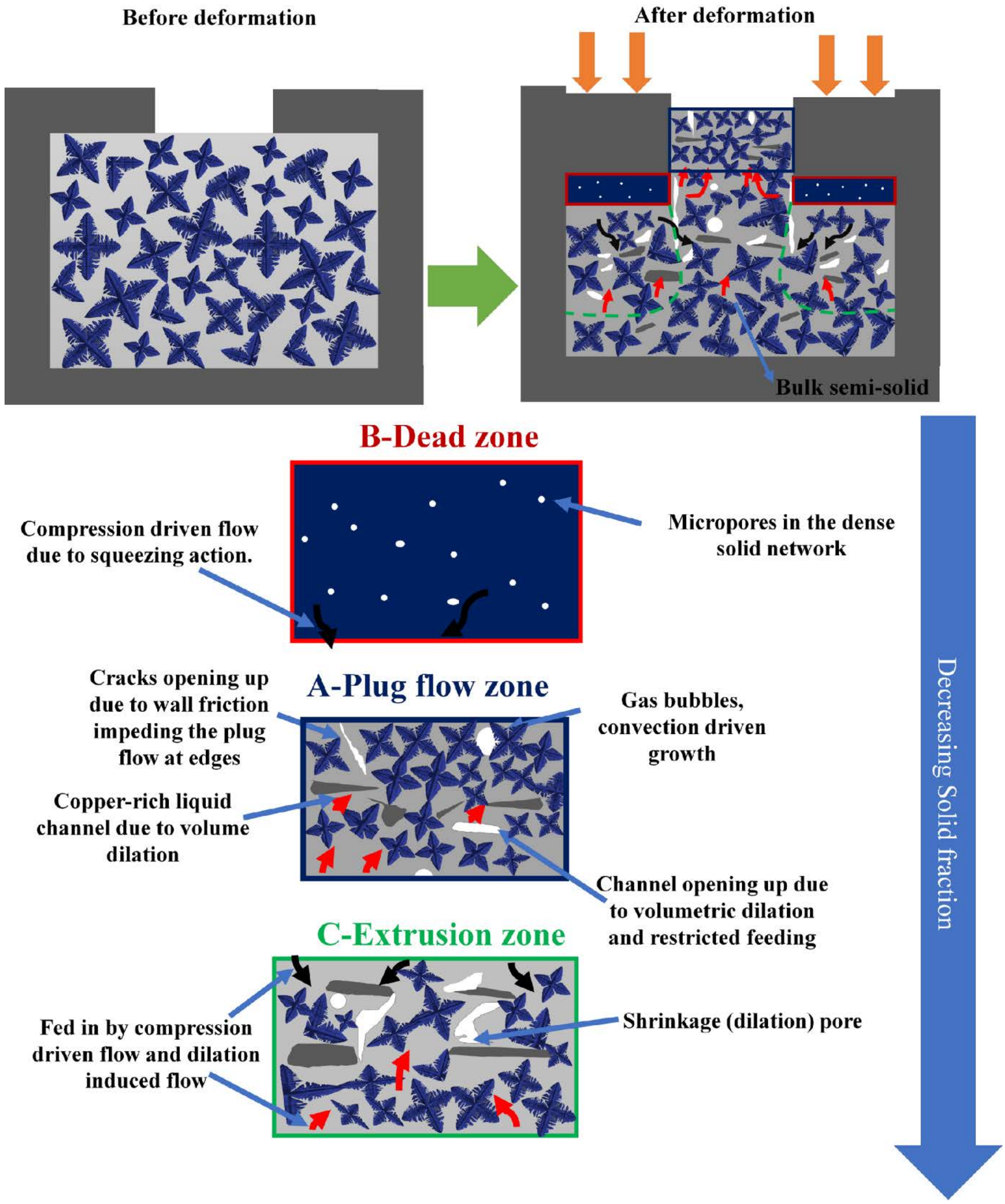

Figure 8: Proposed mechanism for defect formation during injection of semisolid Al alloy at high solid fractions.

The literature on HPDC [58,59] suggests that regions with solid fractions varying from very high (>85-90%) to low (~25-50%) are present simultaneously. These regions of varying solid fractions develop due to the varying thickness in the component, which changes not only the local cooling conditions but also the flow behaviour.

These regions are subjected to shear and compressive forces by the melt injection and movement, high intensification pressure, and shrinkage forces. As explained in Figure 8, in high solid fraction regions, the local segregation and porosity are heavily influenced by the loading conditions. In this study, we have proposed distinct zones to identify the interplay between the aforementioned factors on local microstructures and defect formation. To better predict porosity in HPDC, it is required to develop maps of such zones that correlate the semisolid response to the local stress systems. The process maps produced in these experiments can be combined with macroscale fluid mechanics simulations to optimise HPDC operating conditions and casting geometries, impacting the automotive component manufacturing chain.

4. Conclusions

Using fast *in situ* synchrotron X-ray imaging during semisolid injection experiments, the role of solid fraction, semisolid flow behaviour and stress conditions on the final microstructure and porosity is revealed, in two different Al die-cast alloys, utilising a die with varying cross-sections. The following conclusions are drawn from the investigation:

1. For low solid fractions, the solid is extruded as a network of pinned grains and liquid convects through the inter-dendritic regions. The semisolid flow as a whole shows plug flow characteristics with the interface moving at a constant velocity. Significant remelting was observed at the solid-liquid interface at the end of deformation. The final casting has two distinct microstructural features - coarse grains at the centre surrounded by fine grains at the edges.
2. For higher solid fraction experiments, the nature of defects is determined by the local stress state. In the constriction zone porosity defects were aligned both along and perpendicular to the loading directions. High shear zones developed due to the flow impediment caused by the frictional effects at the wall and development of dilatant shrinkage bands.
3. The area fraction of the porosity was determined from the 3D characterisation of the solidified high solid fraction sample. Based on the local stress state, pore and liquid fraction, four regions of significance were defined: plug flow zone, dead zone, shear zones and the bulk. Mapping of such regions can be used to develop zone-specific strategies to model the defect formation during HPDC.

Acknowledgements:

S.K and P.D.L acknowledge the sanction of the project P1299 under the SPARC (Scheme for Promotion of Academic and Research Collaboration) initiative. The authors thank the University Research Program at Ford Motor Company, USA, for partial financial support. We are grateful to Diamond Light Source for the beamtime

(MG22053-1) and the help of all the staff on the I13-2 beamline. We acknowledge the assistance of Sebastian Marussi in designing the ceramic die-piston arrangement and his help in setting up the rigs for beamtime. We thank G.S. Abhishek and D. Rees for assistance during the beamtime. The support from the ferrous metallurgy and the machine tools laboratories at IIT Bombay to prepare the samples are acknowledged. This work was supported by the Royal Academy of Engineering (CiET1819/10) and Laboratory space and facilities were provided by the Research Complex at Harwell (funded in part through UK-EPSRC grant EP/P006566/1).

References

[1] M.S. Dargusch, A. Hamasaaid, G. Dour, N. Balasubramani, D.H. StJohn, The Influence of In-Cavity Pressure on Heat Transfer and Porosity Formation During High-Pressure Die Casting of A380 Alloy, Jom. (2020). doi:10.1007/s11837-020-04341-y.

[2] E.J. Vinarcik, J. Wiley, High Integrity Die Casting Processes, 1st ed., John Wiley & Sons, INC., 2003.

[3] D. Bernard, Ø. Nielsen, L. Salvo, P. Cloetens, Permeability assessment by 3D interdendritic flow simulations on microtomography mappings of Al-Cu alloys, Mater. Sci. Eng. A. 392 (2005) 112–120. doi:10.1016/j.msea.2004.09.004.

[4] S.G.R. Brown, J.A. Spittle, D.J. Jarvis, R. Walden-Bevan, Numerical determination of liquid flow permeabilities for equiaxed dendritic structures, Acta Mater. 50 (2002) 1559–1569. doi:10.1016/S1359-6454(02)00014-9.

[5] G. Lesoult, C.A. Gandin, N.T. Niane, Segregation during solidification with spongy deformation of the mushy zone, Acta Mater. 51 (2003) 5263–5283. doi:10.1016/S1359-6454(03)00379-3.

[6] A. Zavaliangos, Modeling of the mechanical behavior of semisolid metallic alloys at high volume fractions of solid, Int. J. Mech. Sci. 40 (1998) 1029–1041. doi:10.1016/S0020-7403(98)00011-3.

[7] A.K. Dahle, D.H. StJohn, Rheological behaviour of the mushy zone and its effect on the formation of casting defects during solidification, Acta Mater. 47 (1998) 31–41. doi:10.1016/S1359-6454(98)00342-5.

[8] C.M. Gourlay, A.K. Dahle, Dilatant shear bands in solidifying metals., Nature. 445 (2007) 70–73. doi:10.1038/nature05426.

[9] C.M. Gourlay, H.I. Laukli, A.K. Dahle, Defect Band Characteristics in Mg-Al and Al-Si High-Pressure Die Castings, Metall. Mater. Trans. A. 38 (2007) 11–16. doi:10.1007/s11661-007-9243-1.

[10] K.M. Kareh, C. O'Sullivan, T. Nagira, H. Yasuda, C.M. Gourlay, Dilatancy in semi-solid steels at high solid fraction, Acta Mater. 125 (2017) 187–195. doi:10.1016/j.actamat.2016.11.066.

[11] B. Cai, S. Karagadde, T.J. Marrow, T. Connolley, P.D. Lee, Synchrotron X-ray tomographic quantification of deformation induced strain localisation in semi-solid Al- 15wt.%Cu, IOP Conf. Ser. Mater. Sci. Eng. 84 (2015). doi:10.1088/1757-899X/84/1/012079.

[12] F. Bonollo, N. Gramegna, G. Timelli, High-pressure die-casting: Contradictions and challenges, Jom. 67 (2015) 901–908. doi:10.1007/s11837-015-1333-8.

[13] Q. Wan, H.D. Zhao, J.L. Ge, Effect of micro-porosities on fatigue behavior of aluminum die castings, Isij Int. 54 (2014) 511–515. doi:http://dx.doi.org/10.2355/isijinternational.54.511.

[14] K. Kubo, R.D. Pehlke, Mathematical modeling of porosity formation in solidification, Metall. Trans. B. 16 (1985) 359–366. doi:10.1007/BF02679728.

[15] C. John, Castings, Butterworth Heinemann Publ. Second edi (2003).

[16] P.D. Lee, J.D. Hunt, Hydrogen porosity in directional solidified aluminium-copper alloys:in situ observation, Acta Mater. 45 (1997) 4155–4169. doi:10.1016/S1359-6454(97)00081-5.

[17] R.H. Mathiesen, L. Arnberg, F. Mo, T. Weitkamp, A. Snigirev, Time resolved x-ray imaging of dendritic growth in binary alloys, Phys. Rev. Lett. 83 (1999) 5062–5065. doi:DOI 10.1103/PhysRevLett.83.5062.

[18] K. Bartkowiak, S. Ullrich, T. Frick, M. Schmidt, New developments of laser processing aluminium alloys via additive manufacturing technique, Phys. Procedia. 12 (2011) 393–401. doi:10.1016/j.phpro.2011.03.050.

[19] R.C. Atwood, S. Sridhar, W. Zhang, P.D. Lee, Diffusion-controlled growth of hydrogen pores in aluminium-silicon castings: in situ observation and modelling, Acta Mater. 48 (2000) 405–417. doi:10.1016/S1359-6454(99)00363-8.

[20] H. Yin, J.N. Koster, In-situ Observed Pore Formation During Solidification of Aluminium, Isij Int. 40 (2000) 364–372. doi:10.2355/isijinternational.40.364.

[21] S. Sun, Q. Hu, W. Lu, Z. Ding, M. Xia, J. Li, In Situ Observation on Bubble Behavior of Solidifying Al-Ni Alloy Under the Interference of Intermetallic Compounds, Metall. Mater. Trans. A Phys. Metall. Mater. Sci. 49 (2018) 4429–4434. doi:10.1007/s11661-018-4818-6.

[22] C.D. Sulfredge, L.C. Chow, K. Tagavi, Solidification void formation for cylindrical geometries, Exp. Heat Transf. 3 (1990) 257–268. doi:10.1080/08916159008946389.

[23] D.M. Stefanescu, A. V Catalina, Physics of microporosity formation in casting alloys – sensitivity analysis for Al–Si alloys, Int. J. Cast Met. Res. 24 (2011) 144–150. doi:10.1179/136404611x13001912813780.

[24] O. Ludwig, J.-M. Drezet, C.L. Martin, M. Suéry, Rheological behavior of Al-Cu alloys during solidification constitutive modeling, experimental identification, and numerical study, Metall. Mater. Trans. A. 36 (2005) 1525–1535. doi:10.1007/s11661-005-0244-7.

[25] M. Sistaninia, A.B. Phillion, J.M. Drezet, M. Rappaz, Three-dimensional granular model of semi-solid metallic alloys undergoing solidification: Fluid flow and localization of feeding, Acta Mater. 60 (2012) 3902–3911. doi:10.1016/j.actamat.2012.03.036.

[26] M. Sistaninia, S. Terzi, A.B. Phillion, J.M. Drezet, M. Rappaz, 3-D granular modeling and in situ X-ray tomographic imaging: A comparative study of hot tearing formation and semi-solid deformation in Al-Cu alloys, Acta Mater. 61 (2013) 3831–3841. doi:10.1016/j.actamat.2013.03.021.

[27] C.M. Gourlay, H.I. Laukli, A.K. Dahle, Segregation band formation in Al-Si die castings, Metall. Mater. Trans. A Phys. Metall. Mater. Sci. 35 A (2004) 2881–2891. doi:10.1007/s11661-004-0236-z.

[28] H.I. Laukli, C.M. Gourlay, A.K. Dahle, Migration of crystals during the filling of semi-solid castings, Metall. Mater. Trans. A Phys. Metall. Mater. Sci. 36 (2005) 805–818. doi:10.1007/s11661-005-1011-5.

[29] X. Li, Z. Guo, S. Xiong, Influence of melt flow on the formation of defect band in high pressure die casting of AZ91D magnesium alloy, Mater. Charact. 129 (2017) 344–352. doi:10.1016/j.matchar.2017.05.009.

[30] H. Yasuda, T. Nagira, M. Yoshiya, N. Nakatsuka, A. Sugiyama, K. Uesugi, K. Umetani, Development of X-ray Imaging for Observing Solidification of Carbon Steels, ISIJ Int. 51 (2011) 402–408. doi:10.2355/isijinternational.51.402.

[31] B. Cai, S. Karagadde, L. Yuan, T.J. Marrow, T. Connolley, P.D. Lee, In situ synchrotron tomographic quantification of granular and intragranular deformation during semi-solid compression of an equiaxed dendritic Al-Cu alloy, Acta Mater. 76 (2014) 371–380. doi:10.1016/j.actamat.2014.05.035.

[32] B. Cai, S. Karagadde, D. Rowley, T.J. Marrow, T. Connolley, P.D. Lee, Time-resolved synchrotron tomographic quantification of deformation-induced flow in a semi-solid equiaxed dendritic Al-Cu alloy, Scr. Mater. 103 (2015) 69–72. doi:10.1016/j.scriptamat.2015.03.011.

[33] S. Karagadde, P.D. Lee, B. Cai, J.L. Fife, M.A. Azeem, K.M. Kareh, C. Puncreobutr, D. Tsivoulas, T. Connolley, R.C. Atwood, Transgranular liquation cracking of grains in the semi-solid state., Nat. Commun. 6 (2015) 8300. doi:10.1038/ncomms9300.

[34] B. Cai, P.D. Lee, S. Karagadde, T.J. Marrow, T. Connolley, Time-resolved synchrotron tomographic quantification of deformation during indentation of an equiaxed semi-solid granular alloy, Acta Mater. 105 (2016) 338–346. doi:10.1016/j.actamat.2015.11.028.

[35] S. Bhagavath, B. Cai, R. Atwood, M. Li, B. Ghaffari, P.D. Lee, S. Karagadde, Combined Deformation and Solidification-Driven Porosity Formation in Aluminum Alloys, Metall. Mater. Trans. A Phys. Metall. Mater. Sci. 50 (2019) 4891–4899. doi:10.1007/s11661-019-05378-8.

[36] T.C. Su, C. O'Sullivan, H. Yasuda, C.M. Gourlay, Rheological transitions in semi-solid alloys: In-situ imaging and LBM-DEM simulations, Acta Mater. 191 (2020) 24–42. doi:10.1016/j.actamat.2020.03.011.

[37] T.C. Su, C. O'Sullivan, T. Nagira, H. Yasuda, C.M. Gourlay, Semi-solid deformation of Al-Cu alloys: A quantitative comparison between real-time imaging and coupled LBM-DEM simulations, Acta Mater. 163 (2019) 208–225. doi:10.1016/j.actamat.2018.10.006.

[38] B. Cai, J. Wang, A. Kao, K. Pericleous, A.B. Phillion, R.C. Atwood, P.D. Lee, 4D synchrotron X-ray

tomographic quantification of the transition from cellular to dendrite growth during directional solidification, Acta Mater. 117 (2016) 160–169. doi:10.1016/j.actamat.2016.07.002.

[39] K.M. Kareh, P.D. Lee, R.C. Atwood, T. Connolley, C.M. Gourlay, Revealing the micromechanisms behind semi-solid metal deformation with time-resolved X-ray tomography, Nat Commun. 5 (2014) 4464. doi:10.1038/ncomms5464.

[40] A. De Fanis, Z.D. Peić, U. Wagner, C. Rau, Fast X-ray imaging at beamline I13L at Diamond Light Source, J. Phys. Conf. Ser. 425 (2013). doi:10.1088/1742-6596/425/19/192014.

[41] Z.D. Peić, A. De Fanis, U. Wagner, C. Rau, Experimental stations at I13 beamline at Diamond Light Source, J. Phys. Conf. Ser. 425 (2013) 8–12. doi:10.1088/1742-6596/425/18/182003.

[42] C. Rau, M. Storm, S. Marathe, A.J. Bodey, S. Cipiccia, D. Batey, X. Shi, M.-C. Zdora, I. Zanette, S. Perez-Tamarit, P. Cimavilla, M.A. Rodriguez-Perez, F. Doring, C. David, Multi-Scale Imaging at the Coherence and Imaging Beamline I13 at Diamond, Microsc. Microanal. 24 (2018) 256–257. doi:10.1017/s1431927618013624.

[43] C. Puncreobutr, P.D. Lee, R.W. Hamilton, B. Cai, T. Connolley, Synchrotron tomographic characterization of damage evolution during aluminum alloy solidification, Metall. Mater. Trans. A Phys. Metall. Mater. Sci. 44 (2013) 5389–5395. doi:10.1007/s11661-012-1563-0.

[44] I. Arganda-Carreras, V. Kaynig, C. Rueden, K.W. Eliceiri, J. Schindelin, A. Cardona, H.S. Seung, Trainable Weka Segmentation: A machine learning tool for microscopy pixel classification, Bioinformatics. 33 (2017) 2424–2426. doi:10.1093/bioinformatics/btx180.

[45] J. Schindelin, I. Arganda-Carreras, E. Frise, V. Kaynig, M. Longair, T. Pietzsch, S. Preibisch, C. Rueden, S. Saalfeld, B. Schmid, J.Y. Tinevez, D.J. White, V. Hartenstein, K. Eliceiri, P. Tomancak, A. Cardona, Fiji: An open-source platform for biological-image analysis, Nat. Methods. 9 (2012) 676–682. doi:10.1038/nmeth.2019.

[46] A. Fedorov, R. Beichel, J. Kalphaty-Cramer, J. Finet, J.-C. Fillion-Robbin, S. Pujol, C. Bauer, D. Jennings, F. Fennessy, M. Sonka, J. Buatti, S. Aylward, J. V. Miller, S. Pieper, R. Kikinis, 3D slicers as an image computing platform for thw quantitative imaging network, Magn. Reson. Imaging. 30 (2012) 1323–1341. doi:10.1016/j.mri.2012.05.001.3D.

[47] D. Legland, I. Arganda-Carreras, P. Andrey, MorphoLibJ: Integrated library and plugins for mathematical morphology with ImageJ, Bioinformatics. 32 (2016) 3532–3534. doi:10.1093/bioinformatics/btw413.

[48] R.R. Huilgol, M.P. Panizza, On the determination of the plug flow region in Bingham fluids through the application of variational inequalities, J. Nonnewton. Fluid Mech. 58 (1995) 207–217. doi:10.1016/0377-0257(95)01342-S.

[49] D.N. Smyrnaios, J.A. Tsamopoulos, Squeeze flow of Bingham plastics, J. Nonnewton. Fluid Mech. 100 (2001) 165–189. doi:10.1016/S0377-0257(01)00141-0.

[50] P.D. Lee, A. Chirazi, R.C. Atwood, W. Wang, Multiscale modelling of solidification microstructures, including microsegregation and microporosity, in an Al-Si-Cu alloy, Mater. Sci. Eng. A. 365 (2004) 57–65. doi:10.1016/j.msea.2003.09.007.

[51] J. Dantzig, Solidification, EPFL Press, 2009. doi:10.1201/9781439808030.

[52] S. Karagadde, P. Dutta, A comparison of time-scales governing the interaction and growth of hydrogen bubbles with a solidifying front, Int. Commun. Heat Mass Transf. 79 (2016) 16–20. doi:10.1016/j.icheatmasstransfer.2016.10.014.

[53] J.L. Fife, P.W. Voorhees, The morphological evolution of equiaxed dendritic microstructures during coarsening, Acta Mater. 57 (2009) 2418–2428. doi:10.1016/j.actamat.2009.01.036.

[54] D. Kammer, P.W. Voorhees, The morphological evolution of dendritic microstructures during coarsening, Acta Mater. 54 (2006) 1549–1558. doi:10.1016/j.actamat.2005.11.031.

[55] E. Guo, A.B. Phillion, B. Cai, S. Shuai, D. Kazantsev, T. Jing, P.D. Lee, Dendritic evolution during coarsening of Mg-Zn alloys via 4D synchrotron tomography, Acta Mater. 123 (2017) 373–382. doi:10.1016/j.actamat.2016.10.022.

[56] J. Blaber, B. Adair, A. Antoniou, Ncorr: Open-Source 2D Digital Image Correlation Matlab Software, Exp. Mech. 55 (2015) 1105–1122. doi:10.1007/s11340-015-0009-1.

[57] A.B. Phillion, R.W. Hamilton, D. Fuloria, A.C.L. Leung, P. Rockett, T. Connolley, P.D. Lee, In situ X-ray observation of semi-solid deformation and failure in Al-Cu alloys, Acta Mater. 59 (2011) 1436–1444. doi:10.1016/j.actamat.2010.11.005.

[58] S. Otarawanna, H.I. Laukli, C.M. Gourlay, A.K. Dahle, Feeding mechanisms in high-pressure die castings, Metall. Mater. Trans. A Phys. Metall. Mater. Sci. 41 (2010) 1836–1846. doi:10.1007/s11661-010-0222-6.

[59] C.M. Gourlay, A.K. Dahle, H.I. Laukli, Segregation band formation in Al-Si die castings, Metall. Mater. Trans. A. 35 (2004) 2881–2891. doi:10.1007/s11661-004-0236-z.

Figure Captions

Figure 1: (a) Illustration of the sample (light grey) mounted in the custom alumina die-piston combination (dark grey). (b) Alumina and sample are placed between the rams of the P2R loading rig inside the resistive-heated furnace. (c) Example of the sample temperature profile during the injection experiments, in which the heating and cooling rate were maintained at 0.4 °C/s.

Figure 2: Time-resolved radiographic images (a) just before the application of load; with the loading direction is shown as black arrows, (b) extrusion of the solid network, (c) Copper-rich liquid exudation, (d) start of the remelting during the deformation process of Al10Cu alloy. (e-g) show a magnified view of the evolution of interfaces during the remelting process (supplementary video 1). (h) Simplified phase diagram illustrating the mechanism for the remelting phenomenon. Note that the scale bar for Figures (a-d) measures 1 mm and for (e-g) measures 200 µm.

Figure 3: (a) Vertical tomographic slice of the sample. Note that the representative slice is taken at the axisymmetric plane along the thickness, (b) Magnified view of the TR (see Figure 1) of the solidified sample and the corresponding 3D rendering (parallel to loading axis) showing the microstructural changes between the extruded solid (shown in red) and the copper-rich liquid region (shown in green). ISD plots highlighting the distribution of principal curvatures for (c) Region 1 (middle) and (d) Region 2 (edge) shown in (b). Distribution of Gaussian curvature of (e) middle and (f) side section for the 50% semisolid Al10Cu loaded at 80 µm/s.

Figure 4: (a-c) Radiographic slices showing the evolution of pores and cracks during the deformation of Al10Cu. The red boxes indicate the dead zone, and the blue oval indicates shear cracks. (d-g) Enlarged view of the pores at the interface in the yellow box in (b-c). (h-k) DIC images showing strain maps of the same region, highlighting the role of shear and lateral strains in pore opening. Note that the contrast is adjusted in images (d-f) to improve the DIC results. Note that scale bar for Figures (a-c) measures 1 mm and for (d-i) measures 500 µm.

Figure 5: (a-c) Radiographic slices showing the evolution of pores and cracks during the deformation of Al10Cu with a pre-existing pore (based on trial 1 in Figure 6) (see supplementary video 2) (d) Temporal evolution of major

and minor crack length and area fraction of pore (pre-existing pore). Note that the scale bar for figures (a-c) measures 1 mm.

Figure 6: (a) Porosity quantification along the height of the high solid fraction sample deformed at 80 μm/s. The inset shows a 3D volume rendering of the pores in one of the three samples, which is colour coded to show their size, with red indicating the largest pores and blue the smallest. (b) Division into zones based on the local pore and liquid fraction in which blue and red arrows indicate feeding due to dilation and compression, respectively.

Figure 7: (a) Mechanism for crack initiation and growth due to combined reaction and shearing in the constriction region. (b) Magnified view showing the shear-induced crack developed during the plug flow of the semisolid.

Figure 8: Proposed mechanism for defect formation during injection of semisolid Al alloy at high solid fractions.